

1 Digital Elevation Model (DEM) uncertainty
2 and hazard analysis using a geophysical flow
3 model

4 E. R. Stefanescu¹, M. Bursik², G. Cordoba³, K. Dalbey⁴, M.
5 Jones⁵, A.K. Patra¹, D.C. Pieri⁶, E.B. Pitman¹, and M.F.
6 Sheridan²

7 ¹Department of Mechanical and Aerospace Engineering,
8 University at Buffalo

9 ²Department of Geology, University at Buffalo

10 ³Universidad de Nariño, Colombia

11 ⁴Sandia National Laboratories, Albuquerque, NM

12 ⁵Center for Computational Research, University at Buffalo

13 ⁶Jet Propulsion Laboratory, Caltech, Pasadena, CA, 91109
14 USA

15 May 11, 2011

16 **Abstract**

17 To come soon...

1 Introduction

Numerous workers have explored the use of computational fluid dynamics to produce volcanic hazards maps for a variety of phenomena at a number of volcanoes [Baxter and Gresham, 1997, Calvache et al., 1997, Sheridan et al., 2005]. Hazards maps for ground-hugging flows, such as pyroclastic density currents and lava flows are constructed using a digital representation of the terrain [Takahashi and Tsujimoto, 2000, Dalbey et al., 2008]. Usually these terrain representations are digital elevation models (DEMs). For this type of study, elevation is rightly recognized as the most essential and fundamental of variables in geographic information analysis [Atkinson, 2002].

However, a digital representation of a terrain surface is an approximation of reality and is subject to some degree of error. The error usually is not known in terms of both magnitude and spatial distribution. There are in fact large uncertainties associated with the construction of DEMs. In [Wechsler and Kroll, 2006] it was shown that DEMs contain errors derived from a variety of sources: sampling, measurement and interpolation, and these errors cannot always be well estimated.

The most important part of DEM error propagation analysis is the appropriate characterization of the error within the DEM itself, including information about its distribution and spatial structure [Shortridge, 2001]. DEM vendors generally provide users with a measure of vertical accuracy in the form of the root mean squared error (RMSE) statistic. However many papers have reported on the limitations of a single value of accuracy, stressing that DEM error is spatially variable and autocorrelated [Wechsler and Kroll, 2006, Darnell et al., 2008]. Also the magnitude of the DEM error is closely related to the characteristics of the terrain surface. For example, slope will influence interpolation procedures.

DEM error propagation analysis was introduced to the GIS community in the early 1990s. In the work of Heuvelink et al. [1990], error propagation in calculating slope and aspect was represented using Monte Carlo simulation and Taylor series approximation. It was shown that standard deviations of

49 slope and aspect were higher than expected. The effect of error in the DEMs
50 on the erosion models was emphasized. A method used by Weng [2002] in
51 quantification of the uncertainty of DEMs was to create various DEMs using
52 different interpolation methods and to examine the RMSE from the source
53 map, sampling and measurement error, and the interpolation process. It was
54 concluded that RMSE can be used as a general indicator of DEM uncer-
55 tainty. In recent literature, DEM error without spatial autocorrelation was
56 considered to be a worst-case scenario [Heuvelink et al., 1989, Van Niel et al.,
57 2004, Oksanen, 2006], but no analysis based on terrain morphology and the
58 effect of different DEMs was done. Wechsler and Kroll [2006] developed four
59 different methods for representing the spatial dependence of error through
60 random fields to assess the effect on topographic parameters of the DEM
61 uncertainty. The study showed that uncertainty in the DEM is manifested
62 at higher elevations in local steeper slopes, on both slope and elevation maps.
63 Florinsky [1998] showed that the effect of DEM uncertainty on the accuracy
64 of slope and aspect estimation cannot be determined by using data from
65 topographic maps or field surveys, because accurate derivatives cannot be
66 determined.

67 One key feature of spatial data is the autocorrelation of observations in
68 space. Generally, spatial autocorrelation refers to the correlation between the
69 same attribute at two locations. Observations in close spatial proximity tend
70 to be more related than are observations at larger distance or separation.
71 Errors in spatial data (such as incorrect elevation values assigned to a point)
72 are spatially autocorrelated. The effect of correlated DEM error has been
73 investigated in the literature [Fisher, 1991, Goodchild et al., 1992]. It was
74 shown that not only is error spatially variable throughout a DEM, but within
75 the elevation model the error value of an individual grid cell is related to
76 the error in neighboring cells. Unfortunately, DEM providers do not include
77 information regarding the spatial dependence or spatial relationship of errors.

78 Stochastic modeling uses stochastic conditional simulation to generate
79 multiple equally likely representations of an actual terrain surface. Hunter

80 and Goodchild [1997], Ehlschlaeger and Shortridge [1996] computed a normal
81 distribution of maps or realizations to reproduce the spatial autocorrelation
82 encountered in the original error surface, filtered using a Gaussian convo-
83 lution filter, with kernel sizes derived from autocorrelation analysis of the
84 original error surfaces.

85 Various researchers have applied stochastic techniques to evaluate un-
86 certainty in DEM data. Ehlschlaeger and Shortridge [1996] stochastically
87 simulated error in a DEM to evaluate the impact of DEM uncertainty on
88 a least-cost-path application. Hunter and Goodchild [1997] investigated the
89 effect of simulated changes in elevation at different levels of spatial autocorre-
90 lation on slope and aspect calculations. Hebel and Purves [2008] produced
91 uncertainty surfaces to show the impact of DEM uncertainty on an ice sheet
92 model. Darnell et al. [2008] developed a fuzzy framework to examine the
93 probable and possible uncertainties in classifying landslide hazard.

94 The aim of this paper is to quantify the variation in the output of a
95 computational flow model for block and ash flows, when the model inputs
96 are given as a range of possible uncertainties/values. In particular, we focus
97 on assessing the influence of DEM uncertainties, along with uncertainties in
98 initial size and location of the avalanche, and the internal and bed friction
99 angles. There is uncertainty in all of these inputs and it can be represented
100 using either field data or stochastic methods. The distribution or the range
101 of the parameters can be obtained from laboratory and field instruments for
102 friction angles, and historical records of flow frequency and magnitude for size
103 of the initial failure. Stochastic methods are used to assess the uncertainties
104 in the DEMs. In particular, a perturbation of the elevation based on the
105 measured error model, and also an unconditional stochastic simulation are
106 used [Ehlschlaeger and Shortridge, 1996]. Both methods generate multiple
107 likely representations of the actual terrain, while the second one accounts
108 for the spatial autocorrelation between elevation points. The effect of DEM
109 uncertainty and its impact on the output model is analyzed by constructing a
110 hazards map and performing a "probability analysis" for two volcanoes with

111 different morphology: Galeras Volcano, Colombia, and Mammoth Mountain,
112 CA, USA.

113 We adapt here an approach based largely on the method of Ehlschlaeger
114 and Shortridge [1996], which uses the difference between two independent
115 DEMs to train a Gaussian model of error.

116 2 Methodology

117 In previous work [Stefanescu et al., 2010], the effect of DEMs on the out-
118 put of TITAN2D was investigated by comparing the output (maximum flow
119 depth over the entire simulated time) from different DEMs. These DEMs
120 were obtained from different techniques at different resolution. Two types
121 of analysis were performed: a qualitative analysis and a statistical analysis.
122 The qualitative analysis consisted of a comparison of the footprint of the
123 flow, extended to a pixel based classification. The pixels were classified into
124 inundated and non-inundated classes. For the statistical analysis we per-
125 formed a Kolmogorov – Smirnov test to check if two output datasets differed
126 significantly. The conclusion was that for moderate and smaller scale flows,
127 use of different DEMs affects computation of accurate footprints of the flow.

128 This conclusion motivated us in examining the effect of DEM uncertainty
129 by creating a model of the error and sampling it to create an ensemble of
130 possible terrains. The flow simulation is then run on every member of this
131 ensemble.

132 Naive, cell-by-cell approaches to treating DEM uncertainty quickly lead
133 to the use of thousands if not millions of random variables, resulting in a
134 computationally infeasible problem. On the other hand, the error model
135 described above can be parameterized with one or two random variables.
136 The parametrization methods are based on the assumption that the available
137 DEM is a representation of the terrain to which errors have been added
138 because of instrumental uncertainty. Therefore, the DEM can be assumed
139 to be one of an infinite number of elevation realizations.

140 2.1 Method 1

In this paper, we have available two "types" of DEMs of each mountain, which are used in creating DEM-to-DEM difference maps. Different realizations of the terrain were constructed by adding to one DEM – considered to represent the "true" elevation – a "random" perturbation. Since any two types of DEMs are obtained using different techniques, the difference between them can be added to that which is assumed to be the "true" DEM to give us a set of possible DEMs. Thus, the resulting realizations are consistent with the available set of DEMs. Randomness in the perturbations is created by multiplying the difference map with a normally distributed factor between 0 and 1.

$$R = M + \epsilon \cdot Diff \quad (1)$$

141 where R is a realization of the terrain, M is the DEM that best represents
142 the terrain (the "true" DEM), $Diff$ is the difference map and ϵ is a random
143 variable. In this way we can define a set of DEM realizations using only one
144 random variable.

145 2.2 Method 2

146 *In general, DEMs contain information about both the elevation as well as*
147 *its location. For surface elevation, data at any pixels in the DEM tends to*
148 *be similar to data from nearby pixels. This assumption is made when one*
149 *tries to guess the underlying elevation surface given measured elevation. We*
150 *are also using it as the main idea of Method 2. If more than one DEM*
151 *obtained from different techniques, of the same location are available then*
152 *error maps can be constructed. Most error maps are spatially autocorrelated*
153 *and random fields can be used to represent spatially autocorrelated error.*
154 It derives from geostatistics, where vectors of a random variable $Z(\mathcal{U})$ are
155 used to characterize unknown values, generated by probability distributions
156 which characterize the uncertainty of the random variables. Z represents a
157 continuous random field and \mathcal{U} represents the area covered by the random

158 field. *Depending on the nature of the terrain, the $Z(\mathcal{U})$ may be continuous,*
 159 *differentiable or many-times differentiable.*

The random field function used is implemented in the function *r.random.surface* [Ehlschlaeger and Goodchild, 1994] of GRASS GIS [Mitasova et al., 1996], and generates fields containing cells with a normal distribution (mean of 0.0 and variance of 1.0). The random field function derives its spatial dependence by the use of a filter function. The following equation is used to generate the random fields:

$$Z(\mathcal{U}) = \frac{\sum_v w_{u,v} \epsilon_v}{\sqrt{\sum_v w_{u,v}^2}}, \quad u \in \mathcal{U}, v \in \mathcal{V} \quad (2)$$

$$w_{u,v} = \begin{cases} 1 & : d_{u,v} \leq F \\ \left(1 - \frac{d_{u,v}-F}{D-F}\right)^E & F < d_{u,v} \leq D, u \in \mathcal{U}, v \in \mathcal{V} \\ 0 & : d_{u,v} > D \end{cases} \quad (3)$$

160 where $Z(\mathcal{U})$ is the random field, \mathcal{V} is the set of points affecting the area \mathcal{U} ,
 161 $w_{u,v}$ is the spatial autocorrelative effect between points u and v , v is a random
 162 variable with a mean of 0 and variance of 1, $d_{u,v}$ is the distance between u
 163 and v , D is the minimum distance of spatial independence, E is the distance
 164 decay exponent, and F is a parameter that is helps to capture the terrain
 165 features.

166 Random fields are calibrated to the spatial continuity of the field being
 167 simulated using a correlogram function. The method used to fit the cor-
 168 relogram and to choose the best descriptive parameters of the random field
 169 (the minimum distance of spatial independence, the correlated distance de-
 170 cay exponent and the filter parameter) is a weighted least-square estimator
 171 implemented in GRASS's *r.lags.difference*. After running hundreds of tests
 172 with multiple combinations of D , E and F , we found the best random field to
 173 fit the error map characteristics based on the minimum sum of least squares
 174 difference between the error field's correlogram and a target correlogram. xx
 175 *Figure 1 shows the error map correlogram compared to several correlograms*

176 *closely fitting the error correlogram. It is displayed the dependence of the*
177 *correlation coefficient with the lag distance. From Eqn 3 it can be seen that*
178 *the parameters D , E and F influence the shape/look of the correlogram. The*
179 *main property of the exponent value is to determining the texture of the ran-*
180 *dom surface. Texture will decrease as the exponent value get closer to 1.0.*
181 *Once the parameters are set to a certain value as determined above we are*
182 *able to sample from a normal distribution values for ϵ_v as given in Eqn 2.*
183 *In this way a normal distribution of maps are produced where the mean of*
184 *the distribution represents the original DEM used as the “true” surface. xx*

The correlogram model was then used with sequential Gaussian simulation to generate N error map realizations. Each error realization was added to the “true” DEM to generate equally probable realizations of the topography for the error structure of a DEM under consideration:

$$R(U) = m(U) + m(m(T)) + (m(s^2(T)) \cdot \epsilon) \cdot Z(U) \quad (4)$$

185 where $R(U)$ is a realization of an elevation dataset $m(U)$, T is a group of
186 sets of spatially uncorrelated sample points, ϵ is a random variable with
187 mean 0.0 and variance 1.0, and $Z(U)$ is the random field which captures
188 the autocorrelation between points. The mean and the standard deviation
189 are determined from randomly drawn, spatially independent points scattered
190 across the error map. The error map was generated by subtracting the lower
191 quality DEM from the “true” DEM, and characterizes the error of the lower
192 quality DEM at each point.

193 **2.3 DEM realizations**

194 Many DEM users are aware that DEM uncertainty affects the results of
195 their application, however, in most cases the DEM is accepted as the true
196 representation of the earth’s surface. In this section, the two methods for
197 generating multiple realizations of the terrain are presented for both Galeras
198 Volcano and Mammoth Mountain to test whether it is safe to assume that
199 the representation of topography is acceptable as it is.

200 The motivation for creating realizations of the DEM was to be able to use
 201 the DEM along with other uncertain parameters as uncertain inputs for the
 202 calculation of a hazard map using the computational fluid dynamical model
 203 TITAN2D. One of our working hypotheses is that the DEM contributes a
 204 significant proportion of the variance in simulated flow, hence hazard map
 205 output. For sampling the input parameter space, a Latin Hypercube Sam-
 206 pling (LHS) was implemented.

207 For Galeras Volcano, two test DEMs at 30 m spacing were considered for
 208 our analysis. The SRTM (Shuttle Radar Topography Mission) 30m DEM
 209 was derived by spline interpolation from a 90m DEM of southern Colombia
 210 using radar data collected in 2000, while the ASTER (Advanced Spaceborne
 211 Thermal Emission and Reflection Radiometer) DEM was calculated at the
 212 Jet Propulsion Laboratory using orthorectified imagery from 12 January 2010
 213 (Fig. 2 a). The ASTER dataset was used as a surrogate for the “true”
 214 elevation while the SRTM dataset was used in creating the error model.

215 Two 30-m resolution DEMs derived from independent techniques were
 216 used for Mammoth Mountain. A TOPSAR dataset was considered to be the
 217 “true” elevation, while an SRTM dataset was used in creating the error map.
 218 A rectangular area of approximately 42 kilometers² was defined within the
 219 TOPSAR and SRTM DEMs (Fig. 2 b).

220 For Method 1, sixty-four (64) DEM realizations were created and used as
 221 input parameters for the TITAN2D simulator along with uncertain parame-
 222 ters presented in ???. The input space is defined by seven parameters.

223 For Method 2, realizations of the terrain surface were created by taking
 224 into consideration the spatial autocorrelation of the error. The error map
 225 was obtained by subtracting the elevation of a given DEM from the “true”
 226 elevation at each location. The correlogram for the difference map was cal-
 227 culated to determine the range of spatial dependence of elevation points. We
 228 found that spatial dependence persisted above a threshold value of the cor-
 229 relogram cross-correlation coefficient of 0.4 to a distance of 2500 meters for
 230 Galeras and 2100 meters for Mammoth. To determine the probability distri-

231 bution function (pdf) for the stochastic simulation, 91 sets of spot locations
 232 were selected from the map, each set containing 91 points, all pairs of points
 233 were separated by more than 2500 meters or 2100 meters, respectively. For
 234 each DEM, pdf statistics were derived. The random field parameters were
 235 chosen after testing more than 400 random field parameters for the smallest
 236 difference between the error model correlogram and the random field. This
 237 occurs when the minimum distance of spatial independence, $D = 2500$; the
 238 distance decay, $E = 0.8$, and the filter parameter, $F = 400$ for Galeras and
 239 $D = 2100$, $E = 0.7$, and $F = 350$ for Mammoth. A total of 64 equally prob-
 240 able potential elevation surfaces of the area having a 30-m resolution were
 241 generated.

242 **2.4 Hazard map construction**

243 There are numerous ways to create a volcanic hazards map based on com-
 244 putational fluid dynamics modeling. The traditional Monte Carlo method
 245 can be used if we assume that uncertainty in model input parameters is the
 246 main restriction to our knowledge of future events at a given volcano. This
 247 is the case, for example, if we know that block and ash flows are common
 248 at a given volcano, but it is difficult to know the size or volume of potential
 249 future events. Although Monte Carlo is relatively simple to implement, it
 250 converges slowly and is unaffordable computationally because of the number
 251 of time-consuming simulations. A single TITAN2D run might take 20 min-
 252 utes on a single processor. To obtain three-digit accuracy in the expected
 253 value of a specified function would require a million runs. One million runs
 254 of 20-min calculations running non-stop on 64 processor would take 217 days
 255 [Dalbey et al., 2008].

256 Here, we briefly described the use of an hierarchical emulator that signif-
 257 icantly reduces computational cost; a detailed discussion of the methodology
 258 can be found in Dalbey [2009], Dalbey et al. [2008]. An emulator can be
 259 thought of as a fast surrogate for a single numerical model simulation (a sim-
 260 ulator). We describe the process of computing a hazard map for block and

261 ash flows with uncertain model inputs introduced by Dalbey [2009]. Two-
 262 level construction of a group or ensemble of emulators is used to include
 263 a separation of uncertain inputs and geographic coordinates. The process
 264 starts by identifying the model inputs whose uncertainties will drive the pro-
 265 cess. In our case, the uncertain flow inputs we use are volume and shape,
 266 starting location, basal and internal friction angles, and finally topography,
 267 as given by the DEM. For the resulting eight-dimensional parameter input
 268 space, a Latin Hypercube Sampling was performed to determine parameter
 269 values at which simulations were to be run [Mitasova et al., 1996]. As pri-
 270 ors for the emulator, simulation outputs for each of these input parameter
 271 vectors were stored at 64 grid points.

272 The variable of interest for our application is the field of maximum flow
 273 depth over time for each spatial position, at each of the downsampled input
 274 parameter gridpoints. Tessellations of the geographic coordinate space and
 275 the parameter input space are constructed (we use Delaunay triangulation).
 276 At a designated location, \mathbf{x}^* , of the input parameter plus spatial coordinate
 277 space at which the hazard is to be computed, the covering simplex $S_{\mathbf{x}}^*$ of
 278 the parameter space is identified, and all nodes of that simplex are enumer-
 279 ated, as are all nodes within a neighborhood (two hops in the tessellation)
 280 of the covering simplex nodes. For each such two-hop node, we tessellate
 281 in the spatial coordinates and evaluate all emulators constructed over these
 282 nodes. We average these coordinate space emulators to (the coordinate com-
 283 ponents of) \mathbf{x}^* by barycentric weighting; notice there will be an emulator for
 284 each parameter input sample point. Now in the input parameter space, con-
 285 struct a tessellation of the two-hop nodes and average the emulators to \mathbf{x}^* by
 286 barycentric weighting of the fine-scale emulator. The emulator is now read-
 287 ily and quickly evaluated for each evaluation. The hazard map construction
 288 can now proceed by treating the emulator as a surrogate for the simulator
 289 in the classical Monte Carlo procedure. For any point in the domain we
 290 can now exercise the emulator to get potential flows and hence exceedance
 291 probabilities.

2.5 TITAN2D and flow simulations

TITAN2D was developed for modeling dry geophysical granular flows, such as debris avalanches and block and ash flows. Given a digital elevation map specifying the topography of a volcano and the values of input parameters, including the initial volume of erupted material and the friction angles, TITAN2D calculates the flow depth and velocity at any location throughout the duration of an event. The TITAN2D code combines numerical simulations of a natural granular flow with digital terrain data. It is based on a depth-averaged model for an incompressible granular material governed by Coulomb-type friction interactions [Savage and Hutter, 1989]. The governing equations are obtained by applying conservation laws to the incompressible continuum, providing appropriate constitutive modeling assumptions, and then taking advantage of the shallowness of the flows (flows are much longer and wider than they are deep) to obtain simpler depth-averaged representations [Patra et al., 2005]. The motion of the material is considered to be gravitationally driven and resisted by both internal and bed friction. The stress boundary conditions are: no stress at the upper free-surface and a Coulomb-like friction law imposed at the interface between the material and the basal surface.

The primary factor driving the flow is the component of gravity tangential to the surface, which depends on a local slope computed from the elevation data, hence, the criticality of the DEM to the flow computations. The resulting hyperbolic system of equations was solved using a finite-volume scheme with a second-order Godunov solver. Although many real geophysical flows — such as debris flows — are fluidized, in this study we deal only with granular material that has not been fluidized, such as dome-collapse block and ash flows or rock avalanches initiated by slope instability. The program runs in parallel, using the Message Passing Interface (MPI) to allow communication between multiple processors, increasing computational power, decreasing computational time and allowing use of large datasets. The algorithm uses local adaptive mesh refinement for shock capturing, and dynamic load bal-

ancing for the efficient use of computational resources. Topographic data are included in the simulation through a preprocessing routine in which the digital elevation data are imported. TITAN2D performs flow simulations on a DEM of a desired region, the simulation accuracy being highly dependent on the level of the DEM resolution and quality.

Inputs to the code are the size and location of the initial volume, the internal and bed friction and the DEM. Dalbey et al. [2008] presented several methods for characterizing the effect of input data uncertainty on model output. At that time, efficient methods for representing the uncertainty associated with spatial parameters like terrain elevation were not well understood.

2.6 Bayes Linear Method

The straightforward way to account for uncertain inputs and stochastic forcing is a Monte Carlo approach — run many simulations and ‘average’ the results in some fashion. If simulations are expensive to run, this approach is not feasible. To circumvent this difficulty, the statistics community has developed the idea of an emulator. In essence, the emulator is a regression surface based on a representative sample of simulations at selected inputs, accompanied by statistical error bounds. Equipped with this surface, output values at new (untested) input values need not be run. Instead output results can be determined by evaluating the emulator. There are indeed many methods – kriging, metamodels, support vector machines, etc., by which such surrogates may be constructed and there exists a body of literature on the topic [Simpson et al., 2001, Clarke et al., 2005]. One often-used emulator is the GAuSSian Process (GASP) emulator, which assumes the regression has the form of a trend plus a Gaussian [Kennedy and O’Hagan, 2001, Conti and O’Hagan, 2007, O’Hagan, 2006, Bayarri et al., 2010]. To construct a GASP emulator, the covariance structure of the Gaussian must be assumed and parameters determined by Bayesian or partially Bayesian methodology. A fully Bayesian determination of the emulator can be costly, especially if

the input data is high-dimensional. Here we use the Bayes Linear method (BLM) [Goldstein, 2007] to construct an emulator. Given prior beliefs (B) of mean and variance, the BLM updates these beliefs conditioned on the data (D). Note that “data” generally here refers to the output of computationally expensive physics based simulators. Because only the first two moments of a distribution are determined, the BLM is exact only for Gaussian distributions. As an emulator construction, the BLM update is simpler than a full GASP construction, but the resulting emulator is comparable. Given the prior expectation $E[B]$ and variance $var(B)$, the BLM updates are

$$\begin{aligned} E_D(B) &= E[B] + cov(B, D)(var(D))^{-1}[D - E[D]] \\ var_D(B) &= var(B) - cov(B, D)(var(D))^{-1}cov(D, B) \end{aligned} \quad (5)$$

These update formulae can be derived by minimizing the mean square error $(B - a^T D)^2$ between B and some linear combination of the data. Thus the BLM update can be viewed as the projection of the set of prior beliefs onto the span of the data.

3 Implementation

3.1 Case study I: Galeras Volcano

Galeras Volcano (elevation 4,276 meters), located in southwestern Colombia ($1^\circ 13.31'$ N and $77^\circ 21.68'$ W), is one of the most active volcanoes on the world [Hurtado and Cortes, 1997]. Nearly 400,000 people currently live near the volcano; 10,000 of them reside within the zone of high volcanic hazard. Pyroclastic flows pose a major hazard for this population. The current period of activity that began in 2004 presents a serious problem for all stakeholders: decision makers, scientists, public safety officials, and the general population. Computational modeling has the potential to provide useful information for hazard assessment and risk mitigation. However, there is a need to evaluate the validity of the modeling and the quality of the DEMs available for use in such modeling.

379 Galeras is an important volcano for computational flow modeling from
380 both risk management and scientific perspectives [Calvache et al., 1997].
381 Forecasts of volcanic explosions using various geophysical tools [Narvaez
382 et al., 1997] have occasionally brought public warnings to a high level of
383 alert during the past 20 years. When the alert reaches the highest level,
384 the public are urged to evacuate some local areas; this occurred as recently
385 as January, 2010. The worst event at Galeras occurred in 1993, when an
386 eruption killed 9 scientists and journalists [Baxter and Gresham, 1997].

387 The topography of the volcano presents a problem for creation of a good
388 DEM. The irregular morphology on a small scale, with steep slopes, narrow
389 channels, deep gorges and abrupt cliffs poses problems for the creation of
390 accurate topographic models [Ordoñez Villota and Jentzsch, 2000]. In addition,
391 the current flow hazard map at Galeras is mainly based on the sparse
392 geological record [Calvache, 1990]. Dense vegetation, deep erosion, successive
393 deposits of lava and pyroclastic flows hinder the tracing of specific deposits in
394 the field. The diverse effects of this landscape, as reflected in DEMs created
395 by different processes and of different scales, must be examined and quantified
396 to determine the level of confidence that can be placed in model results.
397 Galeras provides a wide range of topographic features that challenge the use
398 of computational flow models.

399 **3.2 Case study II : Mammoth Mountain**

400 Mammoth Mountain is a large, geologically young, composite dome volcano
401 located on the southwestern rim of Long Valley Caldera, California [Bailey,
402 1989]. There are many active hazards issues for Mammoth Mountain, including
403 snow avalanches, rock avalanches and debris flows. In addition, it is
404 intersected by the Mono-Inyo Craters volcanic chain, which is the most active
405 volcanic region in the southwestern U.S. If Mono-Inyo type activity occurs
406 on Mammoth Mountain, then domes may form. These new domes would
407 be growing atop a steep edifice, and therefore could become gravitationally
408 unstable. Given that block and ash flows occurred at Mammoth Mountain

409 during its older dome growth stage, there is reason to believe that renewed
410 dome formation would result in block and ash flow activity. If this is so, then
411 parts of Mammoth Lakes, CA, are at risk from block and ash flows. Our
412 previous work on Mammoth Mountain (Stefanescu et al., submitted) was
413 the testing of the hypothesis that different DEMs result in different model
414 outputs of block and ash flow inundation.

415 **3.3 Model Set-up**

416 In our process to quantify the DEM uncertainties using TITAN2D, a set of
417 parameters was drawn on which to set the bounds of the input domain: in-
418 ternal friction angle, basal friction angle, flow volume, location and DEM.
419 The numerical values for these parameters were chosen to bracket the range
420 of flow volumes and initial locations, and to be representative of the friction
421 angles that have been used by other researchers in their computational mod-
422 els. The same reasonable parameter values were used for both volcanoes,
423 so they do not necessarily represent any optimization for a particular case.
424 The internal friction angle has little effect on the output of the flow models
425 [Dalbey et al., 2008, Sheridan et al., 2005]. Many TITAN users have chosen
426 values of internal friction that range between 15 and 37 degrees with values
427 between 30 and 35 being the most frequent values used [Patra et al., 2005,
428 Murcia et al., 2010]. For our study we use an internal friction angle uniformly
429 distributed between 20 and 25 degrees.

430 The value of the basal friction angle has a large effect on flow dynamics in
431 the TITAN2D simulations [Patra et al., 2005, Stinton et al., 2006]. Factors
432 that could affect the choice of basal friction angle include the volume of the
433 flow, the type of the pyroclastic flow, the nature of the substrate and the
434 amount of channelization. Murcia et al. [2010] listed the basal friction values
435 chosen by TITAN2D users; they range between 5 and 28 degrees; the mean
436 value being about 15 degrees. We are using a basal friction angle uniformly
437 distributed between 15 and 20 degrees.

Volumes of pyroclastic flows at stratovolcanoes typically cover a few or-

ders of magnitude. The volume values in this study bracket the range of possible pyroclastic flows for both Mammoth and Galeras. According to Calvache [1990], Galeras volcano produced 5 large pyroclastic flow eruptive episodes; an historic eruption in 1866, and prehistoric events in 1100, 2300, 2900, and 4500 yBP. The total deposit volumes of these episodes range from $O(10^6 - 9 \times 10^6)m^3$. Block and ash flows on Mammoth Mountain might contain $O(10^5 - 10^7)m^3$ of material [Patra et al., 2005, Burkett, 2007]. Thus, our choice of volumes ranges from 1.9×10^5 to $5 \times 10^6 m^3$. The shape of the initial failure region is approximated as a paraboloid for which the volume is calculated as follows:

$$V = \frac{\pi}{2} \cdot r_{min} \cdot r_{max} \cdot h_{max} \quad (6)$$

438 For a good match of the volume range, the radius values were uniformly
439 distributed between 25 and 500 m, while the initial height followed the same
440 distribution with values between 10 and 150 m.

441 Initiation locations were taken from previous mapping of vent sites, cou-
442 pled with knowledge of known weak areas within the volcano as indicated
443 by hydrothermal alteration. Around the centers of the separate initiation
444 locations, different starting positions were uniformly distributed in a circle
445 of radius 200 m. A rectangular area of approximative $40 km^2$ was defined
446 around the vent within the available DEMs as the potential run-out area.

447 4 Results and Conclusions

448 One of the goals of our analysis was to understand the effect of the spatial
449 structure of available DEMs on hazard maps. Figure 2 (c) and (d) show the
450 correlograms for the ASTER DEM and the TOPSAR DEM, which are the
451 DEMs considered to best represent the real topography for Galeras Volcano
452 and Mammoth Mountain, respectively. It is apparent that data processing
453 resulted in a smoothing and filtering of the TOPSAR DEM which causes
454 the correlation coefficient to vary smoothly as a function of distance and any

two elevation values. Using a distance between two points of 2000m, for the ASTER DEM the correlation coefficient is 0.6, whereas for the TOPSAR DEM the correlation coefficient is 0.4. This means that elevation values within the ASTER DEM are more highly correlated.

Starting from these premises, we can explain the hazard map output for the cases when the DEM is considered to be an input parameter for the TITAND2D model. Figures 3 (a) and (c) display maps of Galeras of the probability that the flow depth will exceed 0.5 m in the next ten years using Method 1 or Method 2, respectively, to create the terrain realizations.

Figures 3 and 4 show maps at Galeras and Mammoth of the spatially varying lack of confidence in the probability hazard map depicted in Figure 4 (a) and (b), respectively. The lack of confidence is defined as the computed standard deviation of hazard probability σ_P divided by the hazard probability, P . When calculated by standard means, as was done here, the ratio σ_P/P measures the lack of confidence in the statistic, P , due to insufficient re-sampling of the input parameter space.

After a visual inspection of the figures we can conclude that the difference between hazard map outputs is more obvious for Galeras than for Mammoth Mountain. From the lack of confidence figure it is observed that the error is concentrated at flow margins.

For Mammoth Mountain the differences are less obvious, but with important differences again concentrated at the edge of the flow. An illustration of how the probabilities vary for Method 1 compared to Method 2 is shown in Figure 5. We observe in comparing every point where there is a probability of having a flow depth greater than 0.5 m, the results for Galeras show a greater dispersion than do those for Mountain Mountain. When the flow is deep, the probability is high and tends to cluster near unity for both mountains. As the probability decreases, dispersion becomes greater for Galeras. We can conclude that as the topography becomes more highly correlated, one should use a more complex method for creation of topographic realizations such as stochastic Method 2. It appears that the spatial autocorrelation of the ele-

486 vation points influences the hazard map output and a random perturbation
 487 of the elevation such as that used in Method 1 will not capture this effect.

488 One of the conclusions of our previous work was that for moderate and
 489 smaller-sized flows, different representations of the terrain more profoundly
 490 affect computation of an accurate flow footprint. For the present contribu-
 491 tion, we have built a new set of hazard maps for the case when the volume
 492 is low, with a range between $10^4 - 5 \times 10^4$ and for a high volume between
 493 $9 \times 10^6 - 5 \times 10^7$. Since only 517 pixels for Mammoth and 872 pixels for
 494 Galeras were included in the flow footprint for the low-volume case, for any
 495 particular pixel, the probability that the flow would include that pixel tends
 496 toward unity (in the case of pixels within the starting region), or zero (in
 497 the case of any pixel outside of the starting region but still within the foot-
 498 print). Thus the probability plot appears nearly binary, which means that
 499 we have a hazard (flow greater than 0.5m) with either probability ~ 1 or
 500 ~ 0 Figure 6 (a), (b). We observe that there is a significant mismatch of
 501 prediction between the two methods (left upper corner and right lower corner
 502 in both figures) for both volcanoes that can be critical in the case of a haz-
 503 ards or risk assessment. For high-volume flows at Galeras, we observe that
 504 the area of probability greater than zero is much smaller when we are using
 505 Method 2 (topography is correlated) compared to Method 1 (no correlation
 506 of error between topographic points). We do not know the reason for this
 507 counterintuitive effect.

508 The question that we tried to answer next is “What is the effect of the
 509 DEM in constructing a hazard map?”. A quantitative and qualitative analy-
 510 sis is performed for the case when the “original” deterministic DEM (ASTER
 511 30m for Galeras and TOPSAR 30m for Mammoth as in Figure 7) is used
 512 as input parameter for the hierarchical emulator, contrasted with the case
 513 wherein the input is a set of terrain realizations.

514 We compare the hazard maps produced when DEM uncertainty is not
 515 included against maps produced when DEM uncertainty is included. Fig-
 516 ures 8 and 9 show that for Galeras the probability that the flow was deeper

517 than 0.5m varies considerably from the case of no DEM uncertainty. Hence,
 518 the DEM is an important input parameter and the effect of the DEM it is
 519 not diminished by other uncertain parameters or the methodology used. We
 520 observe that the uncertainty of having flow greater than 0.5 m increases to-
 521 wards the flow edge. For Mammoth Mountain, the DEM uncertainty results
 522 in more uncertainty in the flow outline when Method 2 is used. One of the
 523 causes might be that the flow propagates a shorter distance compared to the
 524 original DEM.

525 Because the uncertainty in flow outline increases for the case of Galeras,
 526 where the autocorrelation is higher, we can say that perturbing the DEM is
 527 more important as autocorrelation increases.

528 References

- 529 P.M. Atkinson. Surface modelling: What’s the point? *Transactions in GIS*,
 530 6:1–4, 2002.
- 531 R.A. Bailey. *Geologic Map of Long Valley Caldera, Mono-Inyo Craters Vol-*
 532 *canic Chain and Vicinity, Eastern California*. Department of the Interior,
 533 Reston, VA (US), 1989.
- 534 P.J. Baxter and A. Gresham. Deaths and injuries in the eruption of Galeras
 535 Volcano, Colombia, 14 January 1993. *Journal of Volcanology and Geother-*
 536 *mal Research*, 77:325–338, 1997.
- 537 M.J. Bayarri, J.O. Berger, E. Calder, K. Dalbey, S. Lunagomez, A.K. Patra,
 538 E.B. Pitman, E.T. Spiller, and R.L. Wolper. Using statistical and computer
 539 models to quantify volcanic hazards. *to appear Technometrics*, 2010.
- 540 S.M. Burkett. Geomorphic mapping and petrography of mammoth mountain,
 541 california. Master’s thesis, State University of New York at Buffalo, 2007.
- 542 M. Calvache. Geology and volcanology of the recent evolution of Galeras

- 543 Volcano, Colombia. *Msc. Thesis. Louisiana State University*, page 171,
544 1990.
- 545 M. Calvache, G.P. Cortes, and S.N. Williams. Stratigraphy and chronology
546 of the Galeras volcanic complex, Colombia. *Journal of Volcanology and*
547 *Geothermal Research*, 77:5–19, 1997.
- 548 S.M. Clarke, J.H. Griebisch, and T.W. Simpson. Analysis of support vector
549 regression for approximation of complex engineering analyses. *Journal of*
550 *Mechanical Design*, 127(6):1077–1088, 2005. doi: 10.1115/1.1897403.
- 551 S. Conti and A. O’Hagan. Bayesian emulation of complex multi-output and
552 dynamic computer models. *Research Report No. 569/07, Department of*
553 *Probability and Statistics, University of Sheffield. Submitted to Journal of*
554 *Statistical Planning and Inference*, 2007.
- 555 K. Dalbey. Predictive simulation and model based hazard maps of geophys-
556 ical mass flows. *PhD thesis, Department of Mechanical and Aerospace*
557 *Engineering, University at Buffalo*, 2009.
- 558 K. Dalbey, A.K. Patra, E.B. Pitman, M.I. Bursik, and M.F. Sheridan. In-
559 put uncertainty propagation methods and hazard mapping of geophys-
560 ical mass flow. *Journal of Geophysical Research*, 113:5203–5219, 2008.
561 doi:10.1029/2006JB004471.
- 562 A.R. Darnell, N.J. Tate, and C. Brunsdon. Improving user assessment of
563 error implications in digital elevation models. *Computers, Environment*
564 *and Urban Systems*, 32:268–277, 2008.
- 565 C. Ehlschlaeger and M.F. Goodchild. Uncertainty in spatial data: Defining,
566 visualizing, and managing data errors. In *Proceedings GIS/LIS’94*, pages
567 246–253, 1994.
- 568 C. Ehlschlaeger and A. Shortridge. Modeling elevation uncertainty in ge-
569 ographical analysis. In *Proceedings of the International Symposium on*
570 *Spatial Data Handling, Delf, Netherlands*, pages 9B.15–9B.25, 1996.

- 571 P.F. Fisher. Modeling soil map-unit inclusions by Monte Carlo simulation. *In-*
572 *ternational Journal of Geographical Information Systems*, 5:193–208, 1991.
- 573 I.V. Florinsky. Accuracy of local topographic variables derived from digi-
574 tal elevation models. *International Journal of Geographical Information*
575 *Science*, 12:1:47–61, 1998.
- 576 M. Goldstein. Bayes linear methods I adjusting beliefs: Concepts and prop-
577 erties. *Part 1 of 3 of online tutorial, website:*, 2007.
- 578 M.F. Goodchild, G. Sun, and S. Yang. Development and test of an error
579 model for categorical data. *International Journal of Geographical Infor-*
580 *mational Systems*, 6:87–104, 1992.
- 581 F. Hebel and R.S. Purves. *Modelling DEM data uncertainties for Monte*
582 *Carlo Simulations of Ice Sheet Models*, chapter Quality Aspects in spatial
583 Data Mining, pages 175–196. A.Stein, J.Shi & W.Bijker, CRC Press, Boca
584 Raton, 2008.
- 585 G.B.M. Heuvelink, P.A. Burrough, and H. Leenaers. Propagation of errors
586 in spatial modelling with GIS. *International Journal of Geographical In-*
587 *formation Systems*, 3:4(303–322), 1989.
- 588 G.B.M. Heuvelink, P.A. Burrough, and H. Leenaers. Error propagation in
589 spatial modelling with GIS. In *EGIS90 Proceedings - First European Con-*
590 *ference on Geographical Information Systems (EGIS Foundation: Utrecht,*
591 *The Netherlands)*, pages 453–462, 1990. In Harts J, HFL Ottens & HJ
592 Scholten (eds.).
- 593 G.J. Hunter and M.F. Goodchild. Modeling the uncertainty of slope and
594 aspect estimates derived from spatial databases. *Geographical Analysis*, 1:
595 35–49, 1997.
- 596 A. Hurtado and G.P. Cortes. Third version of the hazard map of Galeras
597 Volcano, Colombia. *Journal of Volcanology and Geothermal Research*, 77:
598 89–100, 1997.

- 599 M.C. Kennedy and A. O'Hagan. Bayesian calibration of computer models.
600 *Journal of the Royal Statistical Society: Series B (Statistical Methodology)*,
601 63(3):425–464, 2001.
- 602 H. Mitasova, J. Hofierka, M. Zlocha, and L.R. Iverson. Modeling topographic
603 potential for erosion and deposition using GIS. *International Journal of*
604 *Geographical Information Systems*, 10:629–641, 1996.
- 605 H.F. Murcia, M.F. Sheridan, J.L. Macias, and G.P. Cortes. TITAN2D sim-
606 ulations of pyroclastic flows at Cerro Machin Volcano, Colombia: Hazard
607 implications. *Journal of South American Earth Sciences*, 29:161–170, 2010.
- 608 L. Narvaez, R. Torres, D. Gomez, G.P. Cortes, H. Cepeda, and J. Stix.
609 Tornillo-type seismic signals at Galeras volcano, Colombia, 1992–1993.
610 *Journal of Volcanology and Geothermal Research*, 77:159–171, 1997.
- 611 A. O'Hagan. Bayesian analysis of computer code outputs: A tutorial. *Reli-*
612 *ability Engineering and System Safety*, 91(10-11):1290–1300, 2006.
- 613 J. Oksanen. *Digital Elevation Model error in terrain analysis*. PhD thesis,
614 Faculty of Science, University of Helsinki, 2006.
- 615 M. Ordoñez Villota and G. Jentzsch. Mediciones GPS como topografía ba-
616 sica para el estudio de microgravedad en el Volcán Galeras, Colombia.
617 *Ingeominas Internal Report (in Spanish)*, 2000.
- 618 A.K. Patra, A.C. Bauer, C. Nichita, E.B. Pitman, M. F. Sheridan, M. Bursik,
619 B. Rupp, A. Webber, L. Namikawa, and C. Renschler. Parallel adaptive
620 numerical simulation of dry avalanches over natural terrain. *Journal of*
621 *Volcanology and Geothermal Research*, 139:1–21, 2005.
- 622 S.B. Savage and K. Hutter. The motion of a finite mass of granular material
623 down a rough incline. *Journal of Fluid Mechanics*, 199:177–215, 1989.
- 624 M.F. Sheridan, A.J. Stinton, A. Patra, E.B. Pitman, A. Bauer, and C.C.
625 Nichita. Evaluating TITAN2D mass-flow model using the 1963 Little

- 626 Tahoma Peak avalanches, Mount Rainier, Washington. *Journal of Vol-*
627 *canology and Geothermal Research*, 139:275–308, 2005.
- 628 A. Shortridge. Characterizing uncertainty in digital elevation models. *Spatial*
629 *Uncertainty in Ecology: Implications for Remote Sensing and GIS Appli-*
630 *cations* (Springer: New York, NY), pages 238–257, 2001. In Hunsaker CT,
631 MF Goodchild, MA Friedl & TJ Case (eds).
- 632 T.W Simpson, J.D. Poplinski, P.N Koch, and J.K Allen. Metamodels for
633 computer-based engineering design: Survey and recommendations. *Engi-*
634 *neering with Computers*, 17(2), 2001.
- 635 E.R. Stefanescu, M. Bursik, and A.K. Patra. Effect of digital elevation model
636 on geophysical flow model output. *Natural Hazards*, 2010. submitted.
- 637 A.J. Stinton, M.F. Sheridan, A. Patra, K. Dalbey, and L. Namikawa. Incorporation of variable bed friction into TITAN2D mass-flow model: Application to Little Tahoma Peak avalanche (Washington). *Acta Vulcanologica*,
638 16(1-2):153–163, 2006.
- 641 T. Takahashi and H. Tsujimoto. A mechanical model for Merapi-type pyro-
642 clastic flow. *Journal of Volcanology and Geothermal Research*, 98:91–115,
643 2000.
- 644 K.P. Van Niel, S.W. Laffan, and B.G. Less. Effect of error in the dem on
645 environmental variables for predictive vegetation modelling. *Journal of*
646 *Vegetation Science*, 15:6:747–756, 2004.
- 647 S. Wechsler and C. Kroll. Quantifying DEM uncertainty and its effects on
648 topographic parameters. *Photogrammetric Engineering & Remote Sensing*,
649 72:108–1090, 2006.
- 650 Q. Weng. Quantifying uncertainty of digital elevation models derived from
651 topographic maps. *In: Advances in Spatial Data Handling*, pages 403–418,
652 2002.

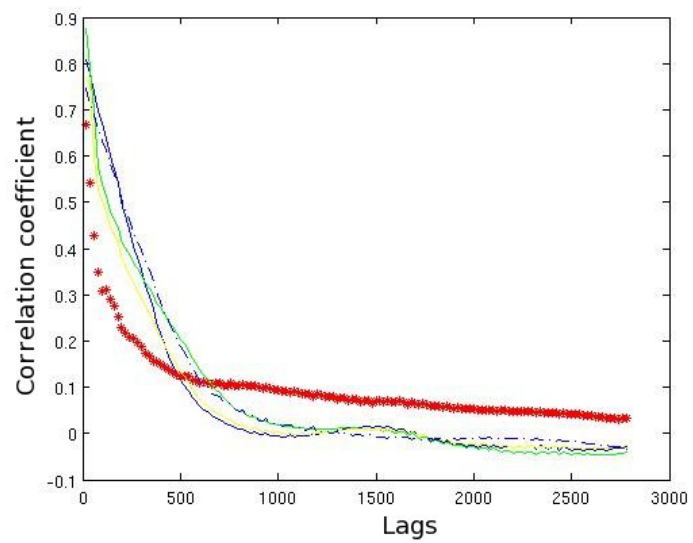
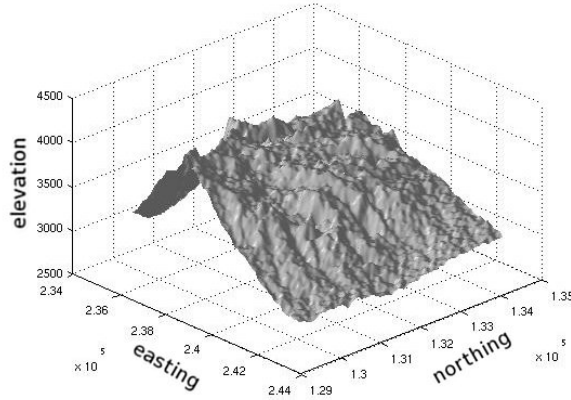
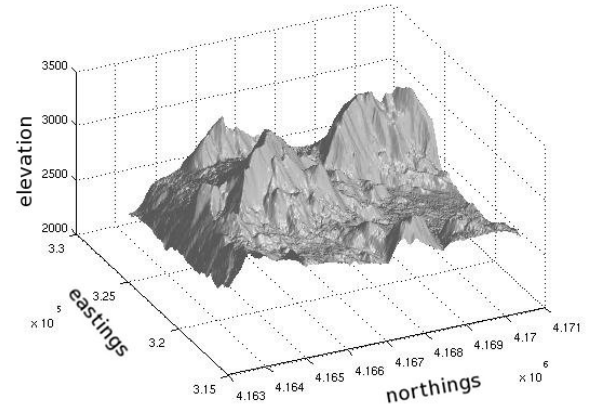


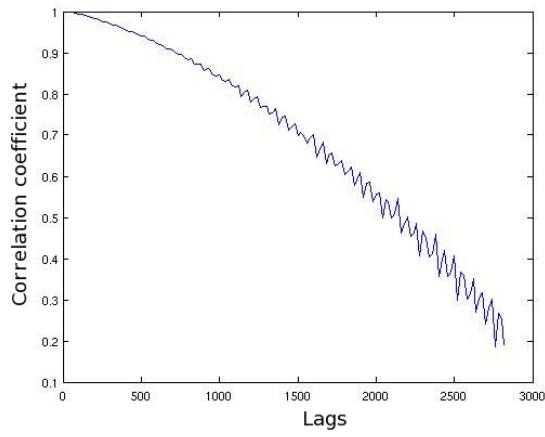
Figure 1: Error map correlogram (red) and various random fields



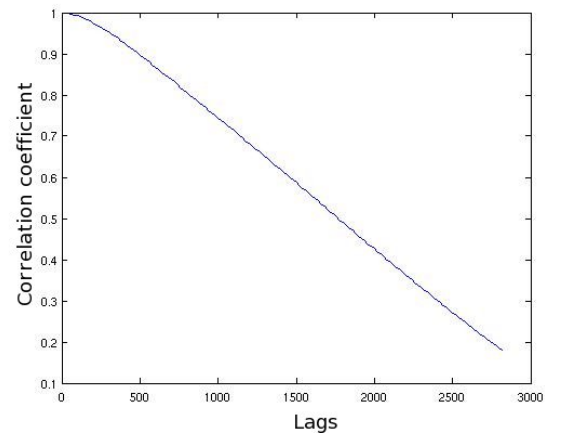
(a)



(b)



(c)



(d)

Figure 2: a) The Galeras ASTER 30m DEM terrain surface (Easting, Northing and elevation coordinates) (b) The Mammoth NED 30m DEM terrain surface (Easting Northing and elevation coordinates) (c) Galeras Volcano ASTER DEM correlogram (d) Mammoth Mountain TOPSAR DEM correlogram

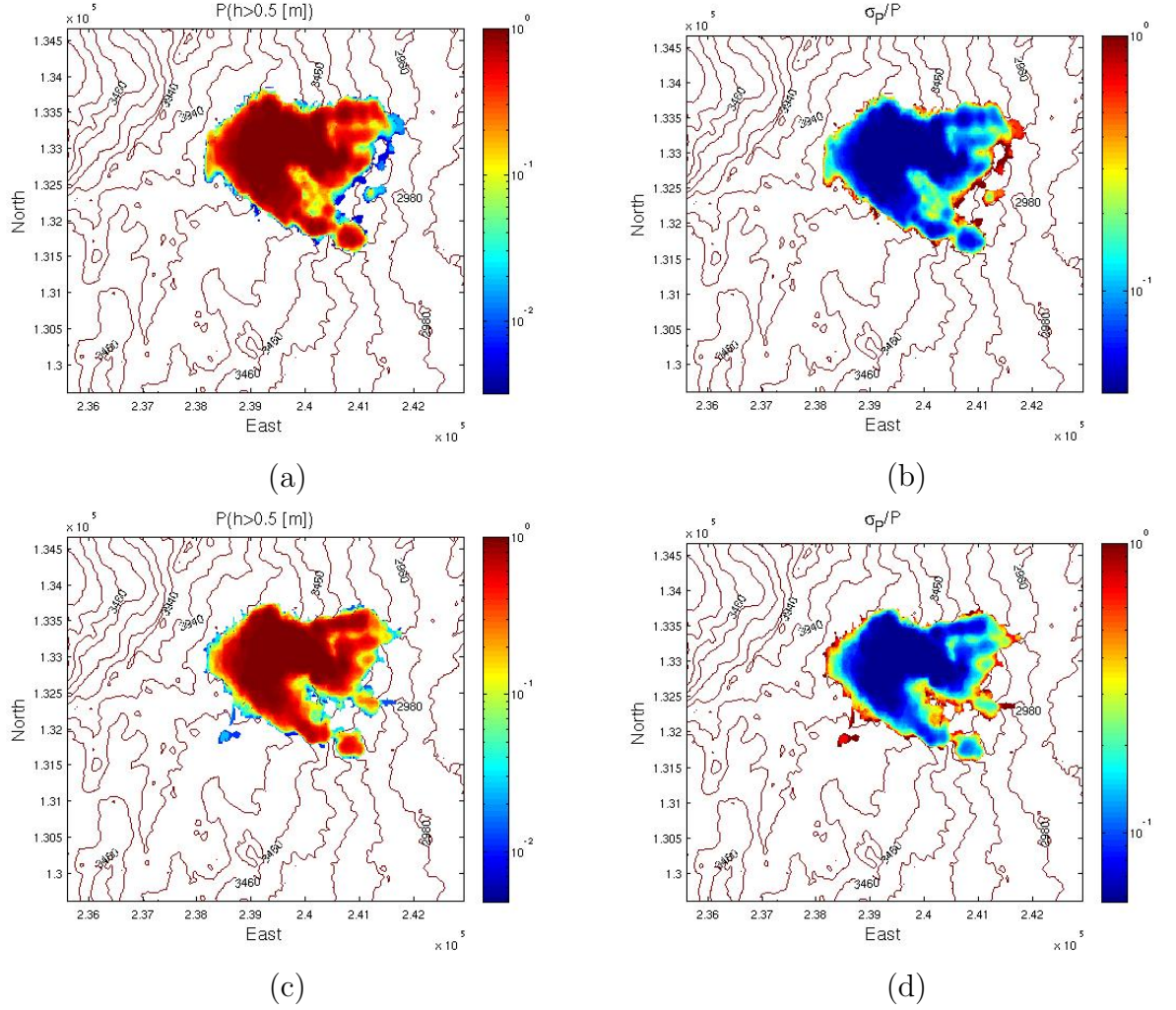


Figure 3: a) Probability that a flow will exceed 0.5 m in depth as a function of position on Galeras Volcano, Columbia, given the uncertainties in DEM and input parameters using Method 1 to create DEM realizations (b) Standard deviation in the estimate that the flow will exceed 0.5 m in depth – Method 1 (c) Probability that a flow will exceed 0.5 m in depth as a function of position on Galeras Volcano, Columbia, given the uncertainties in DEM and input parameters using Method 2 to create DEM realizations (d) Standard deviation in the estimate that the flow will exceed 0.5 m in depth – Method 2

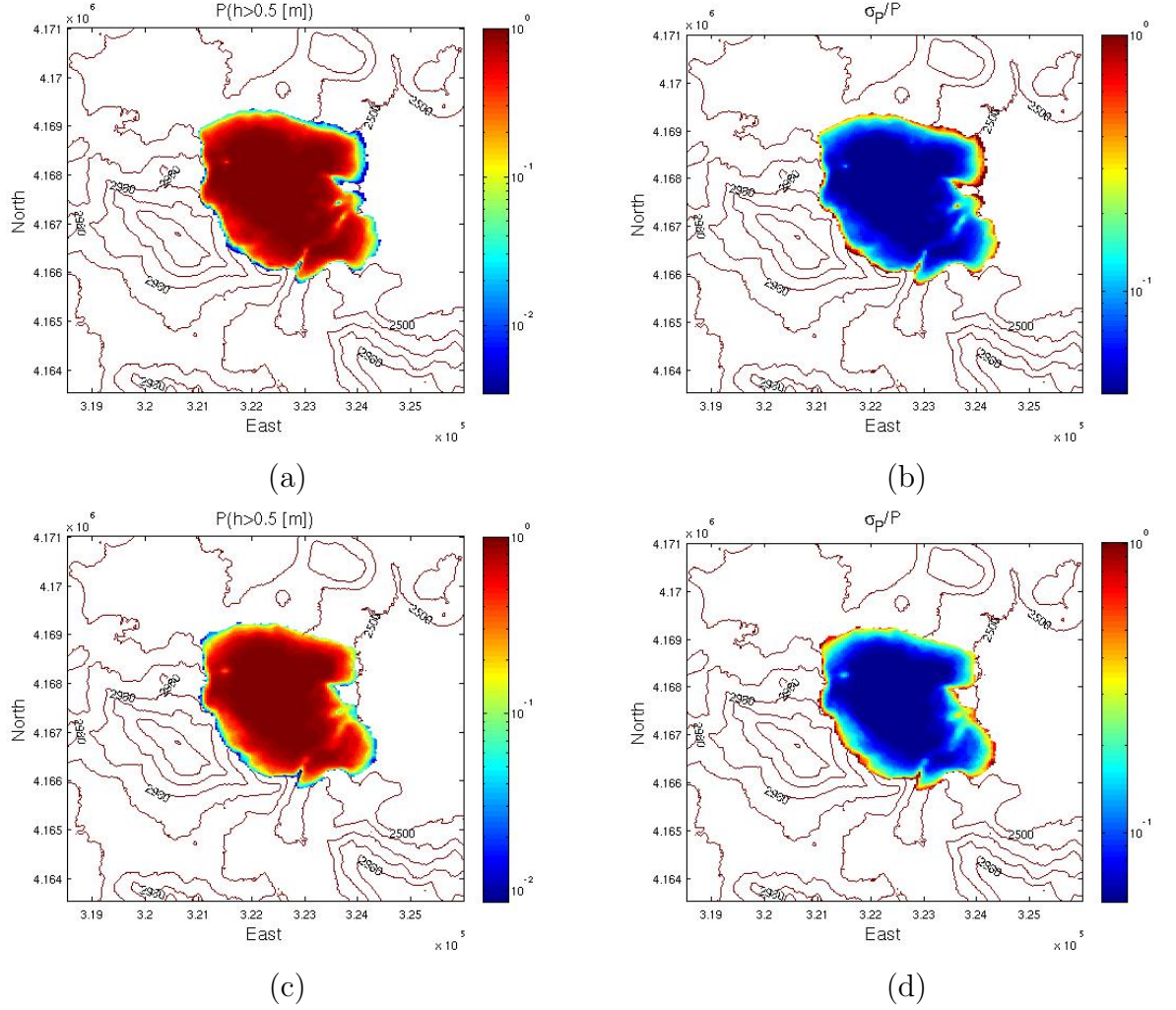
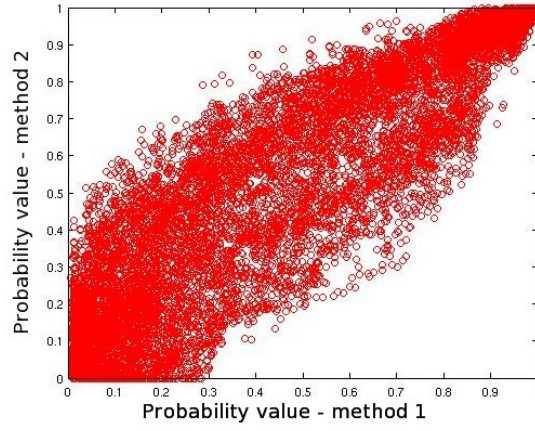
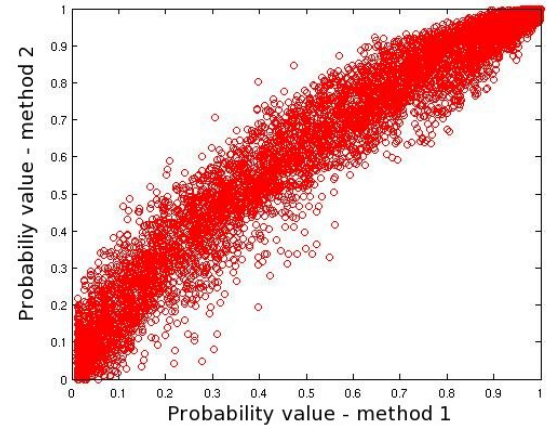


Figure 4: a) Probability that a flow will exceed 0.5 m in depth as a function of position on Mammoth Mountain, CA, given the uncertainties in DEM and input parameters using Method 1 to create DEM realizations. (b) Standard deviation in the estimate that the flow will exceed 0.5 m in depth – Method 1 (c) Probability that a flow will exceed 0.5 m in depth as a function of position on Mammoth Mountain, CA, given the uncertainties in DEM and input parameters using Method 2 to create DEM realizations. (b) Standard deviation in the estimate that the flow will exceed 0.5 m in depth – Method 2

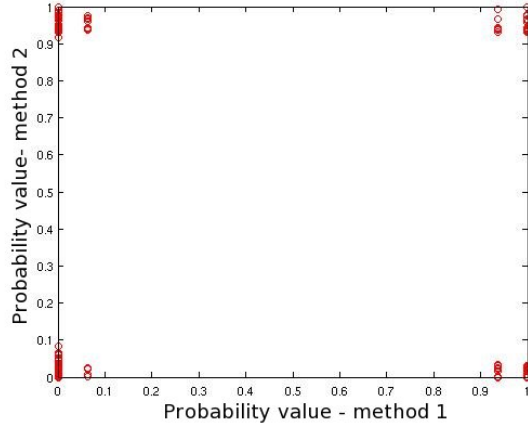


(a)

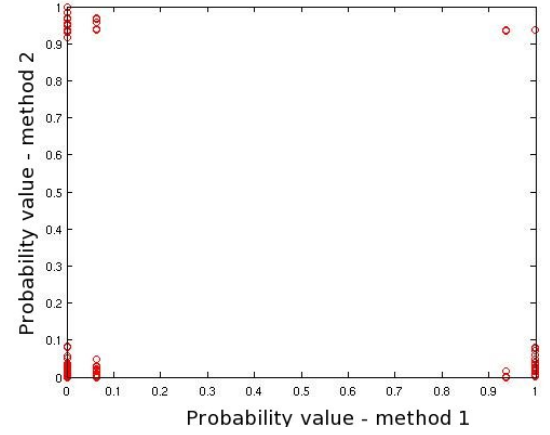


(b)

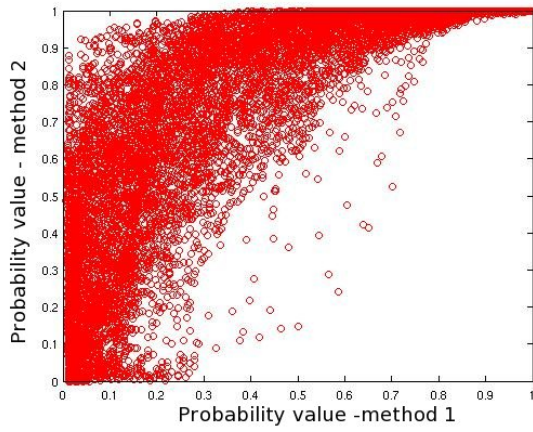
Figure 5: a) The probability that flow will exceed 0.5 m Method 1 versus Method 2 for Galeras Volcano, Colombia (b) The probability that flow will exceed 0.5 m Method 1 versus Method 2 for Mammoth Mountain, CA



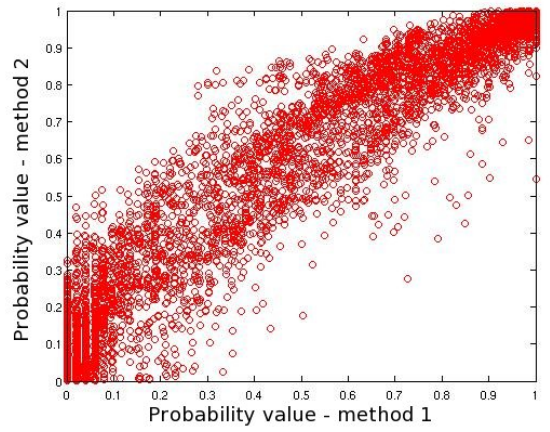
(a)



(b)



(c)



(d)

Figure 6: (a) The probability that flow will exceed 0.5 m Method 1 versus Method 2 for: (a) Galeras Volcano, Colombia for low flow (b) Mammoth Mountain, CA for low flow (c) Galeras Volcano, Colombia for high flow (d) Mammoth Mountain, CA for high flow

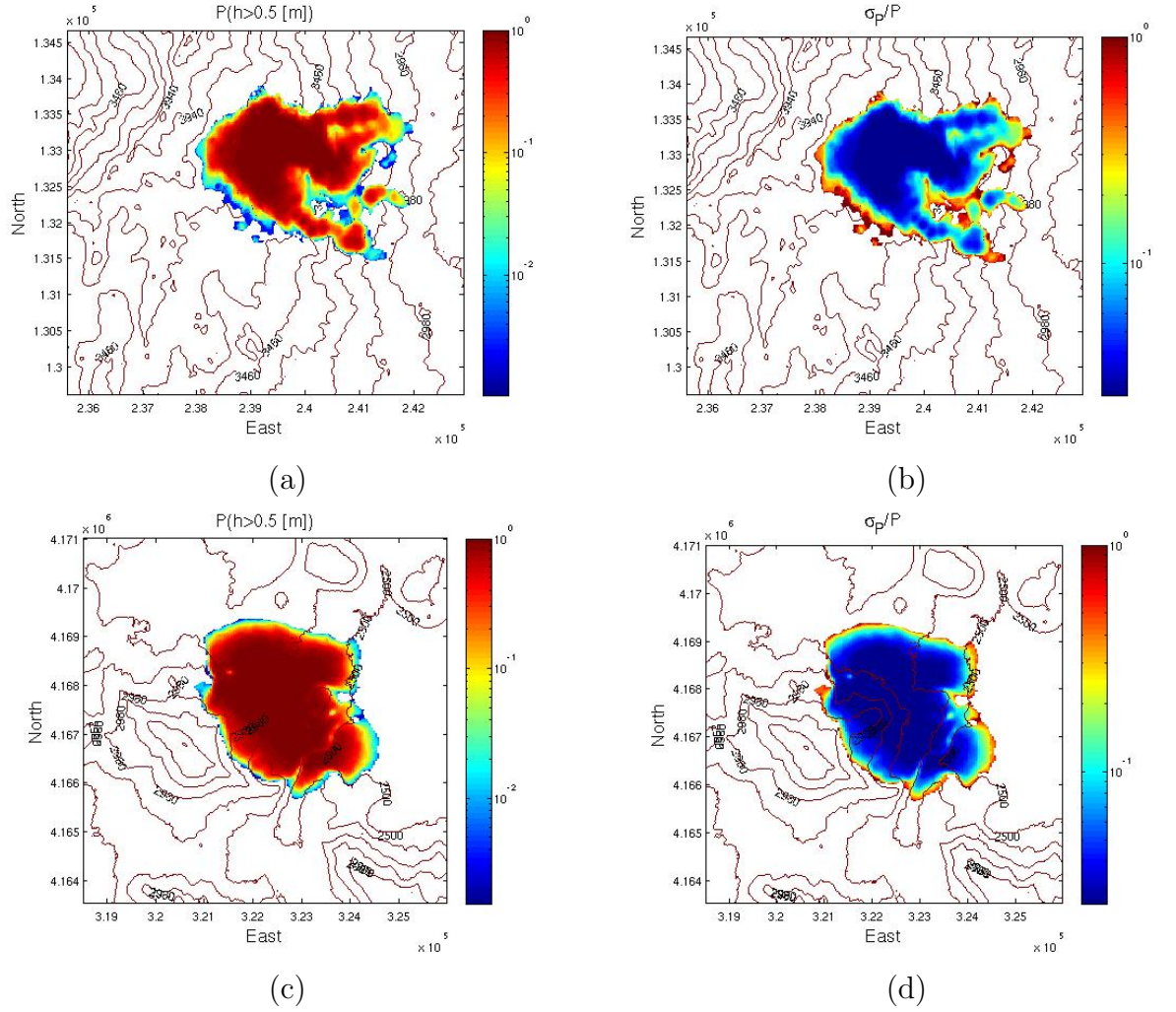
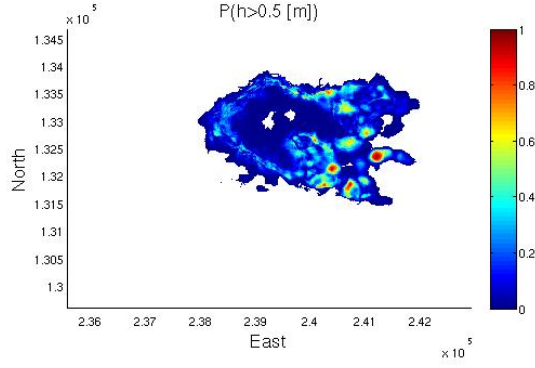
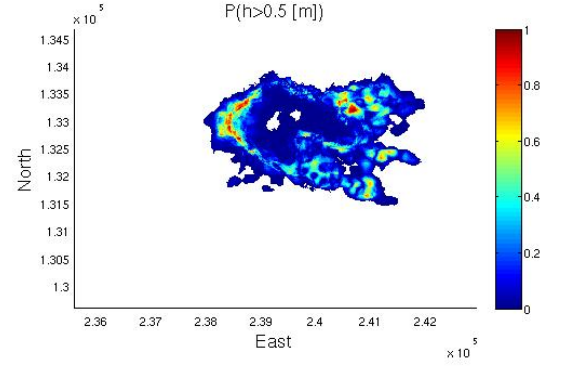


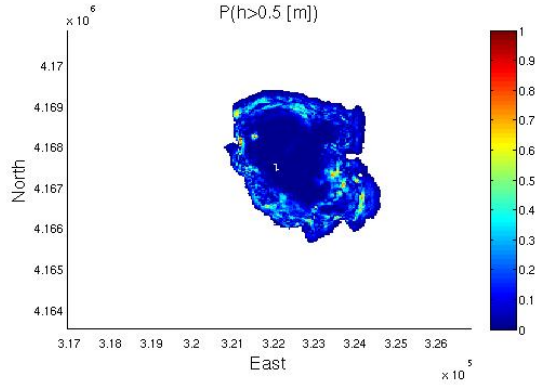
Figure 7: (a) The probability that flow will exceed 0.5 m for Galeras ASTER (b) Standard deviation in the estimate that the flow will exceed 0.5 m in depth for Galeras ASTER (c) The probability that flow will exceed 0.5 m for Mammoth TOPSAR (d) Standard deviation in the estimate that the flow will exceed 0.5 m in depth for Mammoth TOPSAR



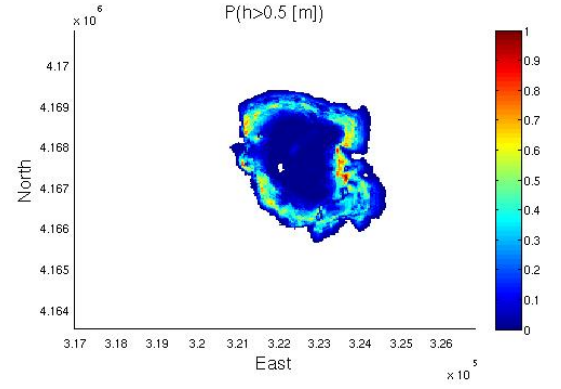
(a)



(b)

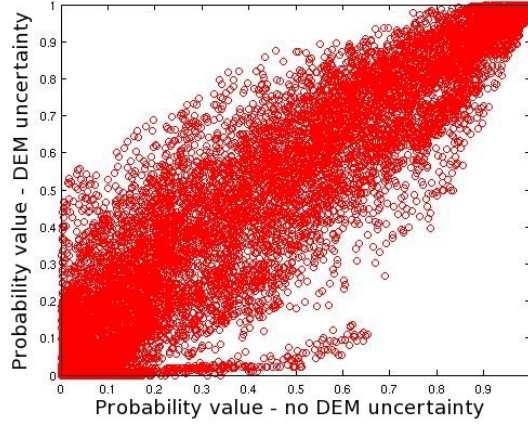


(c)

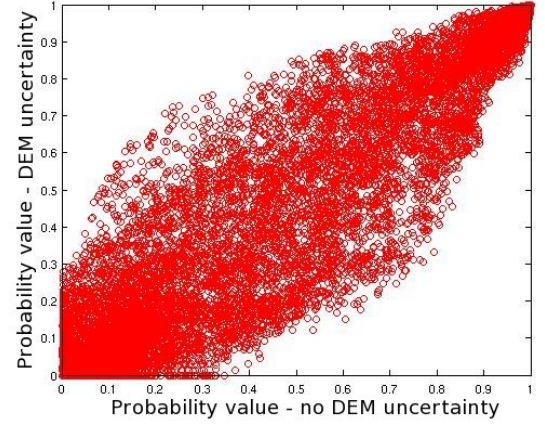


(d)

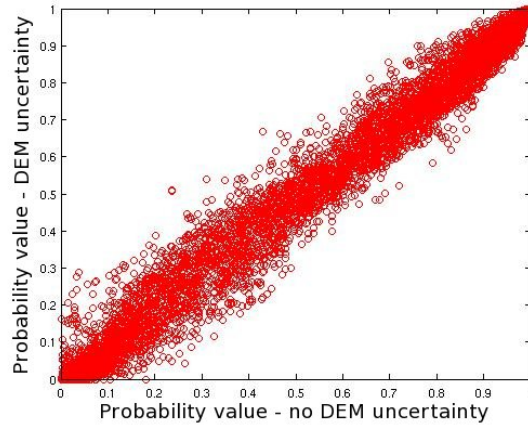
Figure 8: Probability difference map (absolute value) between: (a) Mammoth TOPSAR hazard map and the Method 1 hazard map (b) Mammoth TOPSAR hazard map and the Method 2 hazard map (c) Galeras ASTER hazard map and the Method 1 hazard map (d) Galeras ASTER hazard map and the Method 2 hazard map



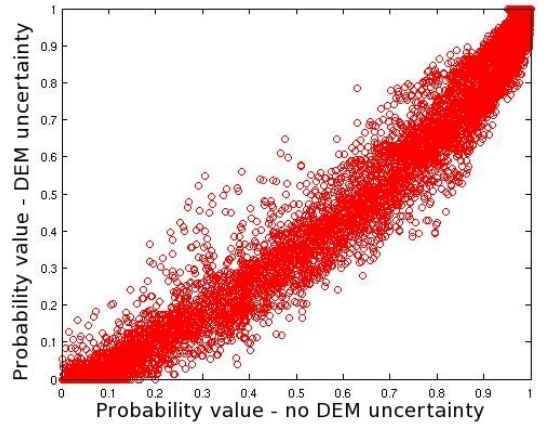
(a)



(b)



(c)



(d)

Figure 9: A comparison of the probability that flow will exceed 0.5 m when we don't assess for the uncertainty in the DEM and when we do, for: (a)Galeras ASTER no DEM uncertainty versus Galeras ASTER DEM uncertainty Method 1 (b)Galeras ASTER no DEM uncertainty versus Galeras ASTER DEM uncertainty Method 2 (c)Mammoth TOPSAR - no DEM uncertainty versus Mammoth TOPSAR - DEM uncertainty Method 1 (d)Mammoth TOPSAR - no DEM uncertainty versus Mammoth TOPSAR - DEM uncertainty Method 2